The Effect of Electrode Shape on Schottky Barrier and Electric Field Distribution of Flexible ZnO Photodiode

Zahra Aminrayai Jezeh
Iran University of Science and Technology
Babak Efafi (babak.efafi@gmail.com)
Iran University of Science and Technology
Bijan Ghafary
Iran University of Science and Technology

Research Article

Keywords: ZnO, Flexible photodiode, Self power, sputtering

Posted Date: May 13th, 2021

DOI: https://doi.org/10.21203/rs.3.rs-499913/v1

Version of Record: A version of this preprint was published at Scientific Reports on August 2nd, 2021. See the published version at https://doi.org/10.1038/s41598-021-95203-3.

The effect of electrode shape on Schottky barrier and electric field distribution of flexible ZnO photodiode

Zahra Aminrayai Jezeh [a], *Babak Efafi* [a,b,*], *Bijan Ghafary* [a]

[a]Photonics Lab, Physics Department, Iran University of Science and Technology, Tehran, Iran.

[b]Nano Photonics Lab, Applied Science Research Center, Kharazmi University, Alborz, Iran.

[*]Corresponding author: babak.efafi@gmail.com

Abstract:

Three metal-semiconductor-metal (MSM) ultraviolet flexible self-powered photodiode (PDs) were fabricated, which differed in the shape of the electrodes. Here, the effect of the electrode's shape on the height of the Schottky barrier and the electric field in these PDs was investigated. They were prepared based on porous Zinc Oxide (ZnO) on fiberglass. Different shapes of the electrodes affect the height of the Schottky barrier in each metal-semiconductor contact and provide the basis for the formation of self-powered PDs. It also affects the electric field generated in the PD's bias condition and affects the PD's parameter. They were fabricated using the radio frequency (RF) sputtering technique, and copper electrodes with different shapes and a sample with interdigitated electrodes were created using the printed circuit board (PCB) method. The photocurrent of the sample with circular and rectangular electrodes was equal to 470 µA in 15V bias, which was twice as good as a sample with an interdigitated MSM structure. It also had the best photocurrent at 0V, which is equal to 0.8 µA. This sample had the best response time among these three samples, which was equal to 440 ms. It is noteworthy that the simulation data confirmed the practical results.

Keywords: *ZnO; Flexible photodiode; Self power; sputtering.*

1. Introduction:

In recent years, the field of flexible and wearable electronic components such as smartwatches, smart glasses and wearable cameras has been growing rapidly. The optical detectors are one of the most important components in wearable electronic devices for measuring light in various applications [1]. Semiconductor materials with wide-bandgap such as ZnO, SiC, GaN, and TiO2 have been used for producing Ultraviolet (UV) PDs and solar cells [2-10]. Among them, ZnO has attracted researchers' attention due to its unique features, including cheapness, high chemical stability, strong radiation hardness, high charge carrier mobility, and most importantly, the 3.37 eV wide-bandgap [3, 6, 11-14]. Ordinary PDs require an external power supply that increases system power consumption, costs, and system volume. This limits the use of these PDs in cases where access is impossible or dangerous [15]. So far, heterojunction contacts, p-n junctions, and Schottky contacts have been used for producing self-powered PDs [16-23].

ZnO PDs are mostly based on MSM because they are controllable, stable, and easy to build. Ordinary MSM PDs, as mentioned, needed an external bias source to generate current. Common MSM structures are made up of two symmetrical Schottky contacts that are connected back to back. Studies have been conducted on MSM devices with two different electrodes (one ohmic contact and one Schottky contact), operating at 0V bias. The production process of these PDs is difficult, and their performance is still not very good. It has recently been shown that the dimensions of electrodes can greatly affect the distribution of the electric field in the Schottky contacts [24]. The electric field can be very effective in separating photogenerated holes and electrons [24]. Thus, a pair of asymmetric electrodes (in terms of material or shape) was used to

produce self-powered ZnO MSM PDs [24-27]. The two asymmetry back-to-back Schottky barriers vary in capability to separate and collect the photogenerated electrons and holes, leading to photocurrent organization in the external circuit without external power supply photovoltaic characteristic [15].

In this work, three flexible self-powered ZnO MSM samples were prepared using RF sputtering technique on the flexible substrate of FR4 fiberglass. We were fabricated porous ZnO because, according to some studies, porous ZnO can improve the PDs parameters [28-31]. It has been reported that porous ZnO thin films prepared by the unbalanced magnetron sputtering method exhibited a fast UV photoresponse [32]. Using the printed circuit board (PCB) method, electrodes with different geometric shapes for samples 1, 2 and interdigitated electrodes for sample 3 were printed simultaneously. The height of the Schottky barrier at the junction of each electrode was examined using MATLAB software. The effect of the difference between these two Schottky barriers on each PD, which is the basis of self-powered PDs, was so investigated. The Schottky barrier height creates an internal potential and thus leads to the carriers' movement. Therefore, it is an important factor in PD parameters.

Also, the geometric shape of electrodes makes a difference in the shape of the produced electric field and the accumulation of charge carriers that will affect their performance. COMSOL Multiphysics software was used to understand the electrodes' shape on the electric field in these PDs.

Analyses illustrate that sample 1 with two different electrodes in a circular and rectangular shape showed the highest current under illumination in the 0V bias, which was equal to 0.8 μA, having a high performance compared to the other self-powered PDs UV [24, 33]. Also, the amount of the

photocurrent is 470 µA at 15V bias and the response time is 440 ms, which shows a much better performance than similar models of symmetrical electrodes, which is due to the difference in heights of the Schottky barrier, the shape of the produced electric field, and accumulation of charge carriers [26, 27, 33].

2. Experimental:

To prepare the samples, ZnO was coated on the FR4 fiberglass substrate using an RF Sputtering at ambient temperature. The FR4 fiberglass was a flexible substrate with a thickness of 0.15 mm. ZnO disk with a diameter of 2 inches (99.99%) was used as the target, and the target-substrate the distance was 10 cm. During the deposition, the sputtering power was set at 150 W, and the Ar pressure was 20 (mTorr). The deposition time was 1945 seconds, and the thickness of the ZnO layer deposited on the fiberglass substrate was about 700 nm. The electrodes were printed on the samples using the PCB method. To apply this method, we plotted the shape of electrodes using Protel software, and the negatives of the design were prepared.

Then the negatives were inserted into the PCB machine for printing. These printed electrodes are made of copper with a thickness equal to 35 µm. In this method, hundreds of samples with different electrode shapes can be prepared at the same time. The structure of these PDs was MSM, where the electrodes were provided in different geometric shapes (Fig.1).

The ZnO layer crystalline properties and its morphology were obtained using the X-ray-Diffraction (XRD) (Fig.2) and the Scanning Electron Microscope (SEM)(Fig.3).

Also, the optoelectronic characteristics of the samples, such as dark current (Fig.4 (a)), photocurrent (Fig.4 (b)), and response time (Fig.5) were measured.

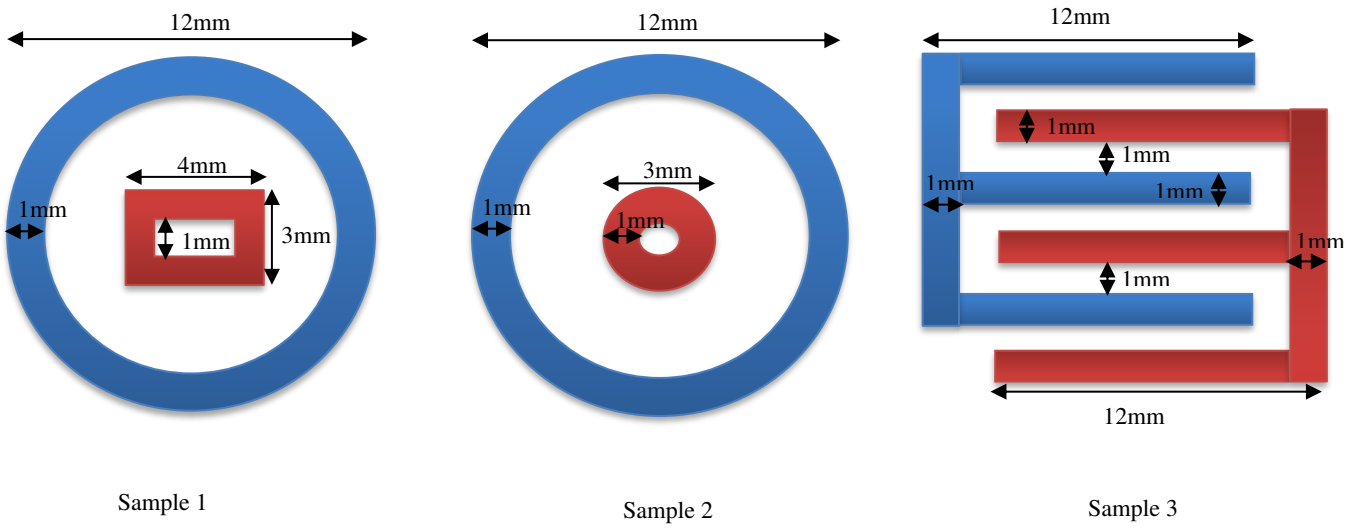

Sample 1 Sample 2 Sample 3

Fig.1: Dimensions of PD electrodes

3. Results and Discussion:

ZnO thin films' phase pattern is determined using XRD at room temperature with a PANalytical PW3050/60 diffractometer using Cu Ka radiation at 40 kV and 40 mA. The XRD pattern was obtained from phase 2θ, from 20° to 80° with a scan rate of 0.03 deg/sec. ZnO diffraction peaks are indexed as (100), (002), (101), (102), (110), (103), and (112) for corresponding peak positions of 32.47∘, 35.066∘, 37.02∘,48.46∘, 57.58∘, 63.73∘, and 69.12∘ (Fig.2). Six hexagonal ZnO peaks can be seen after 30°. The peaks of the spectra correspond to the wurtzite structure of ZnO. The crystal phase identification was performed using ZnO's standard table (JCPDS 65-3411). This film is polycrystalline and has a preferred crystallographic orientation in the (002) plane along the c-axis perpendicular to the substrate surface. The proof for the peak growth in (002) is due to other studies' deposition conditions [34-36].

SEM images of ZnO's thin layer with the fiberglass substrate show the ZnO layer's porosity (Fig.3). As can be seen, the porous layer is well-formed. A porous layer is used since other studies have shown that porosity can benefit detector parameters [28-31].

The work of porous ZnO in the PD can show that the porous vacant in the ZnO layer trap neutral oxygen and increase the response rate due to the neutral oxygen implanted in the grain boundaries in a porous ZnO [32]. The high UV photoelectric response can also be attributed to the high specific surface area. The optoelectronic response performance of ZnO nanomaterials is usually based on their surface state, which causes the upward band to bend close to the surface and trap holes [30, 37]. In the dark condition, oxygen molecules absorb ZnO nanomaterials' surface and deplete electrons, creating a thin depletion layer with low electrical conductivity. Electron-hole pairs are created by UV illumination. The holes move to the ZnO surface due to the bending band and discharge of the adsorbed oxygen molecules, leading to the aggregation of electron concentrations and increasing the electrical conductivity. This particular structure increases absorption. This specific surface area also causes response quickly to the applied light illuminated to the ZnO surface.

In other words, the effect of oxygen is that it captures free electrons in dark conditions and trap holes in illumination, increasing the life cycle of photogenerated carriers and improving the photoelectric response performance of ZnO porous films [30].

In addition to this, in the SEM image, the electrodes and the ZnO layer exist together, which means the electrodes are well arranged on the substrate (Fig.3 (a)).

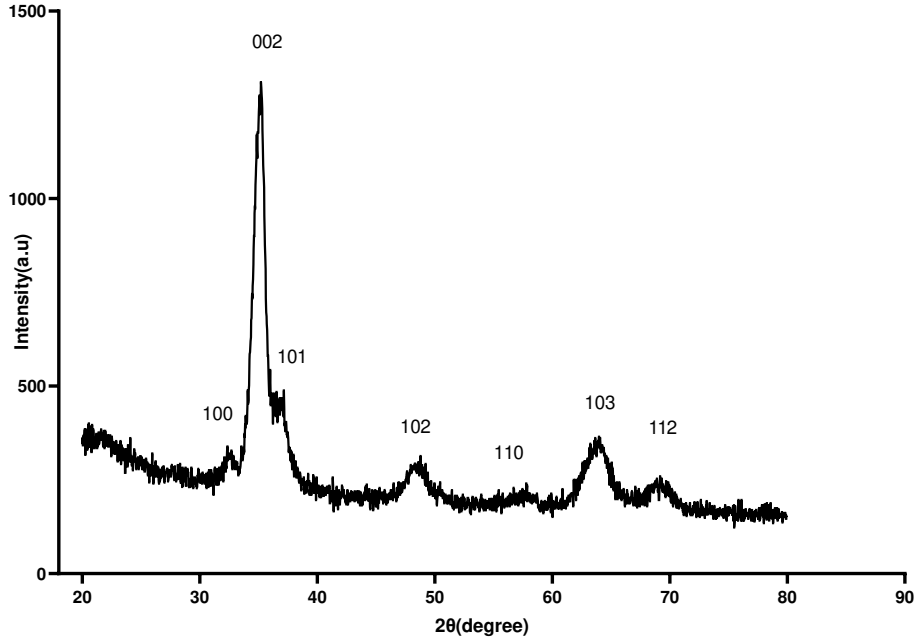

Fig.2: XRD Pattern of flexible UV PDs based on ZnO on the fiberglass (FR4) substrate.

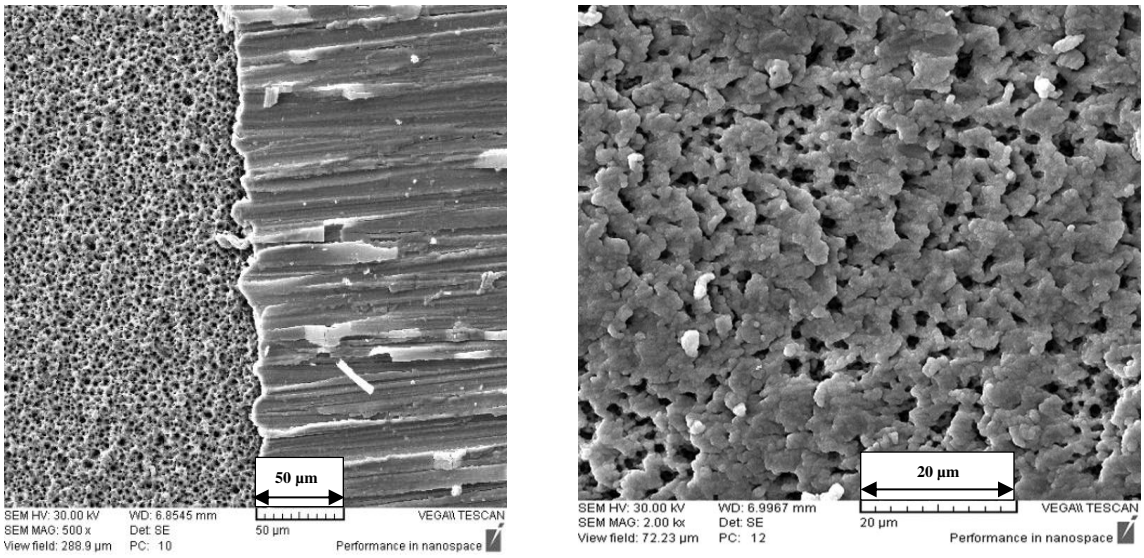

(a) (b)

Fig.3: SEM image of flexible UV PDs based on ZnO on the fiberglass (FR4) substrateat (a) at ×500 magnification of electrode and ZnO together, (b) at ×2 K magnification of ZnO

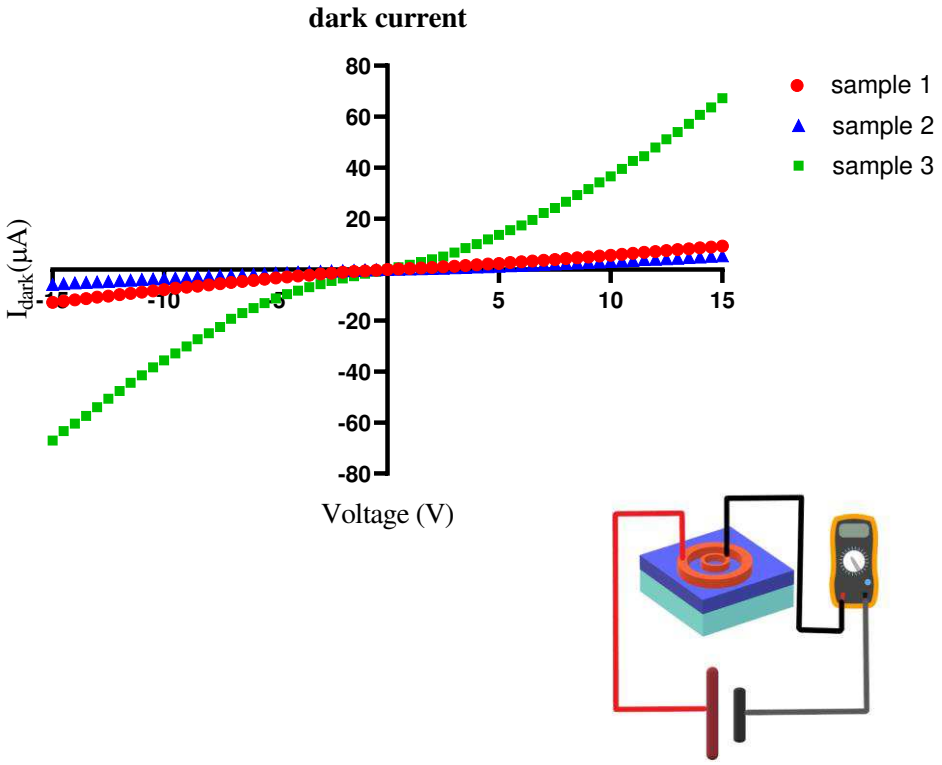

(a)

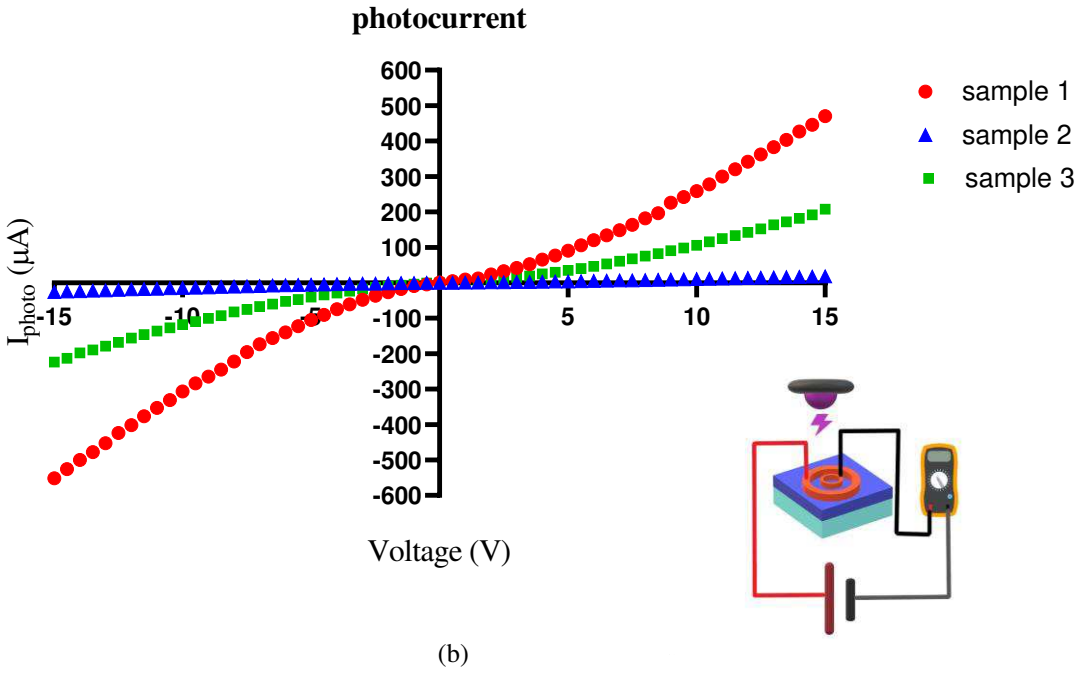

(b)

Fig.4: (a) dark current (b) photocurrent of flexible UV PDs based on ZnO on the fiberglass (FR4) substrate

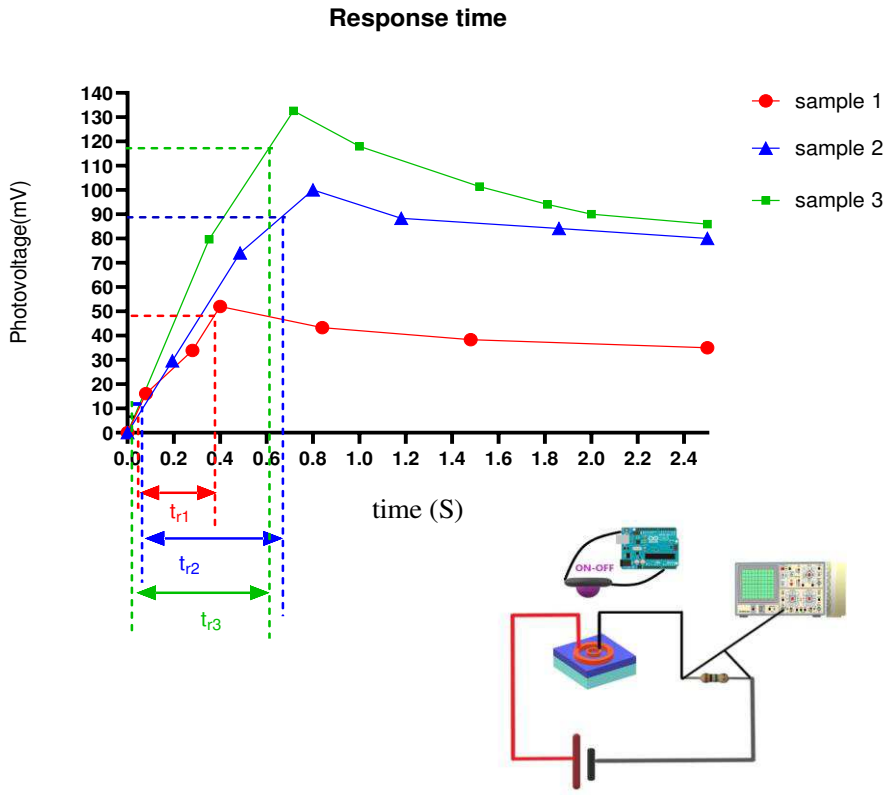

Fig.5: response time of flexible UV PDs based on ZnO on the fiberglass (FR4) substrate

Samples 1 and 2 have a special photovoltaic property in 0V bias due to the electrodes' asymmetry, and both specimens can be called self-powered PDs [15]. To explanation this, the height of the Schottky barrier was calculated [24]. In general, in a Schottky contact, if the $E_{00} << K_BT$, the thermionic emission overcomes the junction electronic transport process without tunneling, where K_B is the constant of Boltzmann, T is absolute temperature, $\left| E_{00} \right|$ is the energy-dependent on the probability of tunneling [38-41]. E_{00} can be calculated using equation (1):

$$E_{00}=(q\hbar/2)\ (N/m^{*}\varepsilon_s)^{1/2} \qquad (1)$$

Where q is the elementary charge, ħ is the reduced Plank constant, N is the carrier density, m^* is the effective mass, and ε_s is the relative dielectric permittivity. In this work, $m_e= 0.27\ m_0$, and ε_s =8.3 for ZnO, and the carrier concentration N is about 9.3×10^{16} cm^{-3}. E_{00} is about 2.2 meV for the

ZnO films, much smaller than the thermal energy K_BT at room temperature (26meV). Thus, the current passing through the Schottky barrier can be described as follows:

$I=I_0\exp(qv/nK_BT)[\ 1-\exp(-qv/K_BT)]$ (2)

$I_0= AA^* \exp(-q\phi_B/K_BT)$ (3)

Where K_B is the Boltzman constant, T is the absolute temperature, n is the ideality factor, A is the junction area, A^* is the Richardson constant ($A^*= 4\pi m^* q^2/h^3$), ϕ_B is the barrier height, h is the Plank constant, and I_0 is the reverse saturation current [24].

The flow passing through the Schottky barrier's height is obtained in a metal-semiconductor contact equation (2). Equation 2 can also be rewritten as follows:

$$\frac{I\exp[qV/kT]}{\exp[qV/kT]-1} = I_0\exp[qV\ /\ nkT] \qquad (4)$$

Based on equation 4, the plot of $\mathrm{Ln}\frac{I\exp[qV/kT]}{\exp[qV/kT]-1}$ Vs. V results in a straight line, $\mathrm{Ln}(I_0)$ is derived from the interception with the y-axis (Fig.6) [42].

After calculating I_0 for each connection, the value of I_0 is placed in equation (3), and the height of the Schottky barrier ϕ_B for each metal-semiconductor connection is obtained. For each of the PDs, the Schottky barrier's height was obtained corresponding to each one and is given in Table 1. The value of I_0 was obtained for each electrode-ZnO connection using MATLAB software from diagram of. Fig.7 shows a view of MATLAB software and the calculation of I_0. P_2 in Fig.7 is $\mathrm{Ln}(I_0)$.

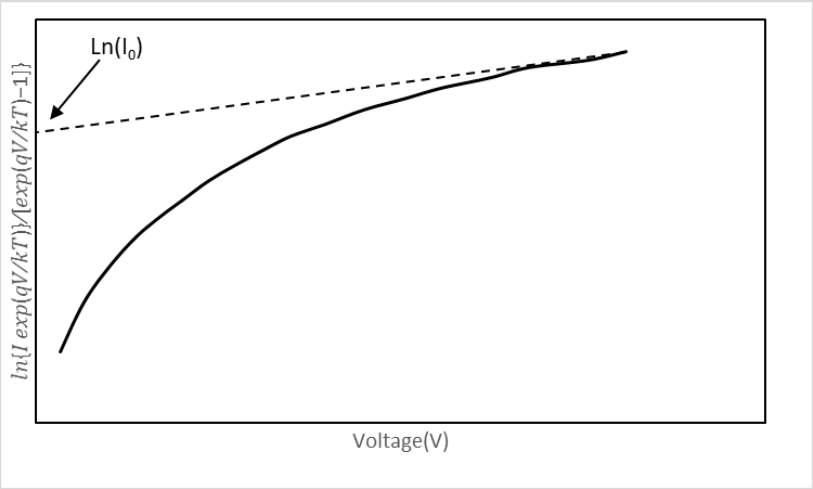

Fig.6: Ln{I exp(qV / kT)} / [exp(qV / kT) − 1]} vs.V of a MSM PD

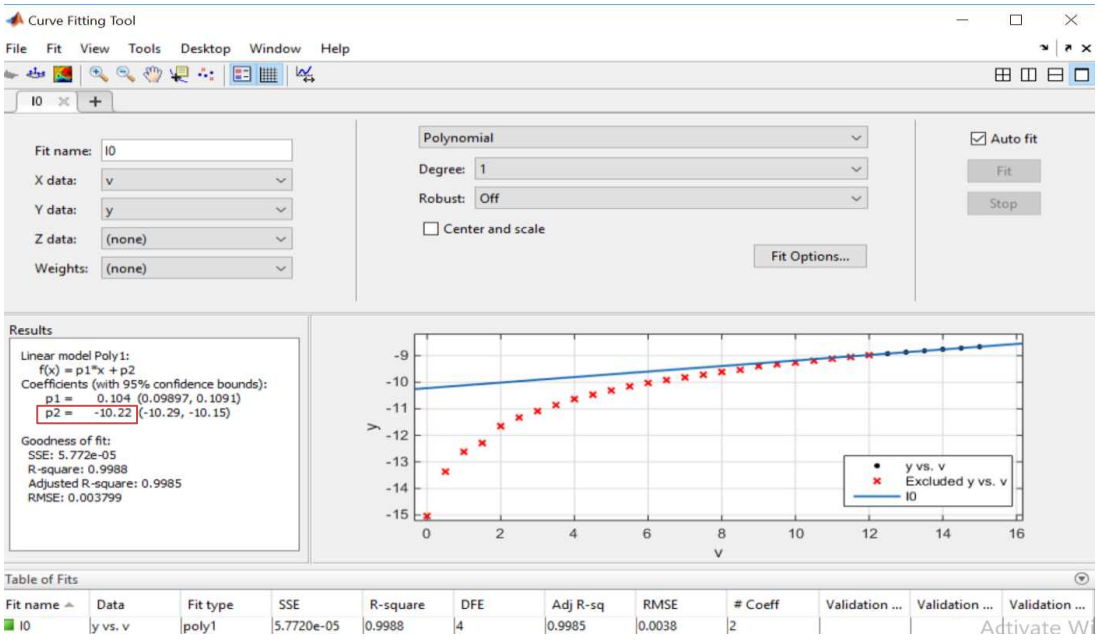

Fig.7: curve fitting in MATLAB software and obtain Ln (I_0)

Based on the energy band theory, the energy band diagrams for samples 1,2 under both dark and UV light illuminated conditions are analyzed and illustrated in Fig.8 (a) and (b,c), respectively. In the dark, the Fermi energy levels (E_F) of ZnO and the electrode are equal. According to the theory calculations [43-45], the width of the depletion region on the Cu (big)-ZnO interface must be greater than the width of the depletion region on the Cu (small)-ZnO interface. Under ultraviolet

light, electron-hole pairs are generated on ZnO's surface, as exhibited in Fig.8 (b). The electrons in the conduction band (E_c) tend to flow away from the metal-semiconductor interfaces, and the holes in the valence band (E_v) move towards the contact. Collected and trapped holes create a local potential in the interface so that the effective height of the Schottky barrier decreases due to the difference in the width of depletion region between Cu (big)-ZnO and Cu (small)-ZnO, and asymmetric distribution of electric potential in ZnO film can induce the difference in separation and transfer of carrier. Since the number of collected and trapped holes in the two interfaces, which reduces the height of the Schottky barrier between two electrodes of Cu (big)-ZnO and Cu (small)-ZnO, which because the number of holes in The Cu (big) -ZnO interface is larger, so the Schottky barrier height reduction is greater (Fig.8 (c)) [46]]. As a result, typical photovoltaic specifications can be seen in asymmetric MSM PDs at a bias voltage of 0V (samples 1,2). It is worth noting that the change in the height of the barrier is highly dependent on ZnO's electrical properties and the Cu electrodes' structure, which can determine the local potential [16, 24, 33, 38, 47-50].

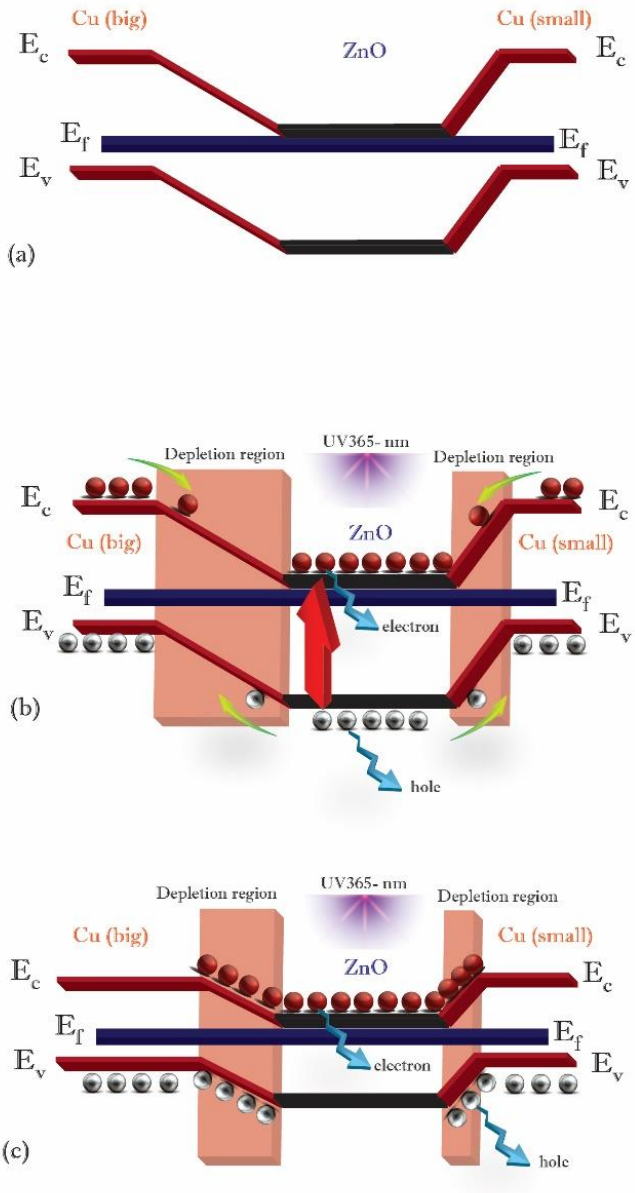

Fig.8: Energy band diagrams of the asymmetric MSM PD at 0 V in the (a) dark and (b, c) illuminated

When a bias voltage is applied between two electrodes, an electric field is created and causes the charge carriers to move, which leads to the production of current. The difference in the electrodes'

shape leads to the difference in the electric field's shape and amount. As a result, the dark current (Fig.4 (a)), photocurrent (Fig.4 (b)) and response time (Fig.5) also vary. To show the influence of an electric field in the organization of electric charges, the electric displacement field is defined [51]:

$$D=\varepsilon_0\varepsilon_r E \qquad (5)$$

Where ε_0 is the vacuum permittivity, ε_r is the relative (dielectric) permittivity, and E is the electric field. The question arises that we do not have the values ε_0 and ε_r. What should we do? The answer is that since ε_0 and ε_r are related to the material, and all three of our samples are the same material, therefore ε_0 and ε_r are the same for all three of our samples, And because our work is comparative, the amount does not matter to us. Based on equation 5, the difference in E leads to the difference in D.

We used COMSOL multiphysics software to obtain the electric displacement field, electric field, and total electric energy. As mentioned, the amount of current caused by charge carriers' movement is directly related to the electric field (E) and the electric displacement field (D).

The electric field and electric displacement field simulation results at 15V bias and total electric energy are given for all three samples (Fig.9). Electric current results from electric charge movement around a circuit, but to move electric charge from one electrode to another, there needs to be a force to create the work to move the electric charge. The total electric energy is defined:

$$J=V.C \qquad (6)$$

J is the total electric energy, V is the voltage, and C is the electric charge.

The total electric energy at the same voltage for these samples was as follows (Fig.9 (c, f, i)):

$J_2 < J_1 < J_3$

J (J) in 15 V are:

$58\times10^{-13} < 83\times10^{-13} < 77\times10^{-12}$

Based on Equation 6, at the same voltage, we have:

C2 < C1 < C3

As seen in Fig.9, The order of the maximum of the E (V/m) and the D (C/m^2) at bias 15 V are as follows:

E_2 (2969.96) < E_1 (4000.05) < E_3(10444.4)

D_2 (8.06×10^{-7}) < D_1(2.15×10^{-6}) < D_3(5.53×10^{-6})

In the dark, the issue of the Schottky barrier and local potential difference is not raised. In table 1, dark current (μA) at bias 15 V:

I_{D2} (5.41) < I_{D1}(9.24) < I_{D3}(67.3)

In general, current means the movement of charge carriers regardless of what is due. According to the statements, the greater the electric displacement field that causes the carriers to move, the greater the current.

As a result, it can be seen that the simulation confirms our experimental data. Under illuminated, in addition to the electric field, the local electric potential, which is caused by the electrodes' asymmetry, is also involved. As a result, these two factors must be considered together. Our experimental results, the highest electric current under illuminated in sample 1, exceeded it in

sample 3. As we learn from the basic concepts of electromagnetism, the electric field is more intense in the sharp points. As a result, the electric field's intensity in those areas is more intense can see in Fig.9 (a, b); at the corners of the rectangular electrode, the density of electric field lines is higher. As a result of both the shape and the amount of electric field, as well as the asymmetry of the electrodes and the creation of a local potential difference, illuminated current (μA) at bias 15 V for PDs are:

I_{illu2} (18.14) < I_{illu3}(208) < I_{illu1}(470)

The local potential difference due to the electrodes' asymmetry creates an electric field that helps compensate for the smaller electric field amount in sample 1 compared to sample 3. As a result of these two factors, sample 1 surpass sample 3. In sample 2, because its field is much smaller than samples 1 and 3 (therefore, it has the lowest amount of dark current) and its local potential difference due to the electrodes' asymmetry could not compensate, so it is observed. Which also has the lowest amount of current under illuminated.

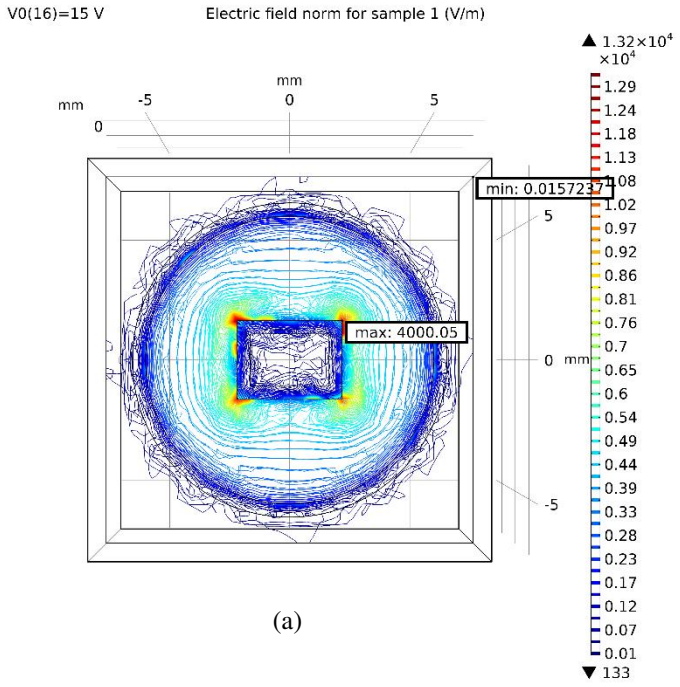
V0(16)=15 V
Electric field norm for sample 1 (V/m)
mm
-5
0
5
mm
0
min: 0.015723
max: 4000.05
5
0 mm
-5
▲ 1.32×10^4
×10^4
1.29
1.24
1.18
1.13
1.08
1.02
0.97
0.92
0.86
0.81
0.76
0.7
0.65
0.6
0.54
0.49
0.44
0.39
0.33
0.28
0.23
0.17
0.12
0.07
0.01
▼ 133

(a)

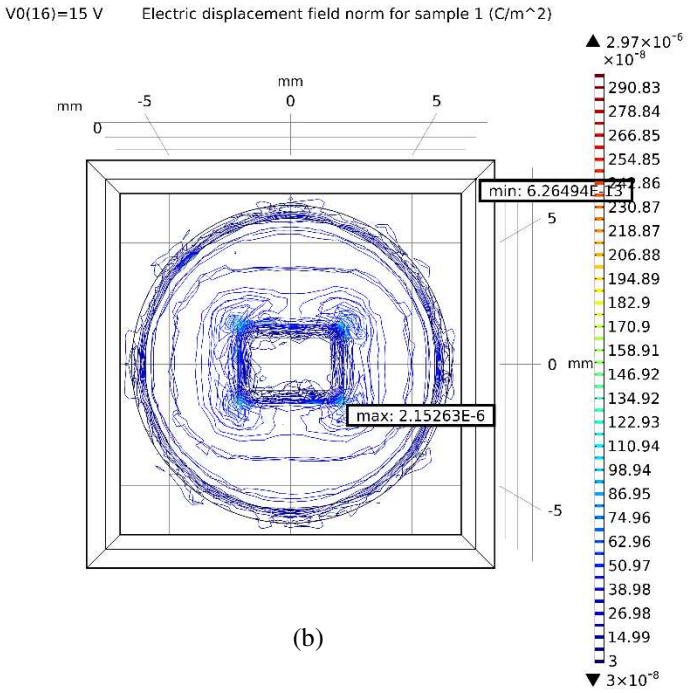
V0(16)=15 V
Electric displacement field norm for sample 1 (C/m^2)
mm
-5
0
5
mm
0
min: 6.26494E-13
max: 2.15263E-6
5
0 mm
-5
▲ 2.97×10^-6
×10^-8
290.83
278.84
266.85
254.85
242.86
230.87
218.87
206.88
194.89
182.9
170.9
158.91
146.92
134.92
122.93
110.94
98.94
86.95
74.96
62.96
50.97
38.98
26.98
14.99
3
▼ 3×10^-8

(b)

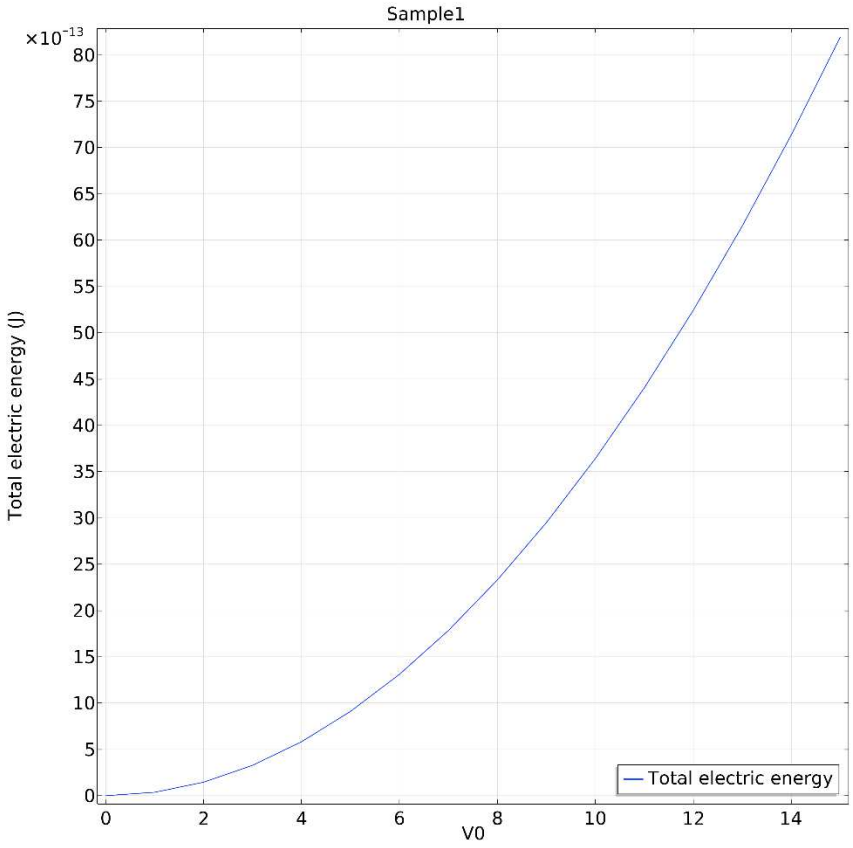
Sample1
×10^-13
Total electric energy (J)
80
75
70
65
60
55
50
45
40
35
30
25
20
15
10
5
0
0
2
4
6
8
10
12
14
V0
Total electric energy

(c)

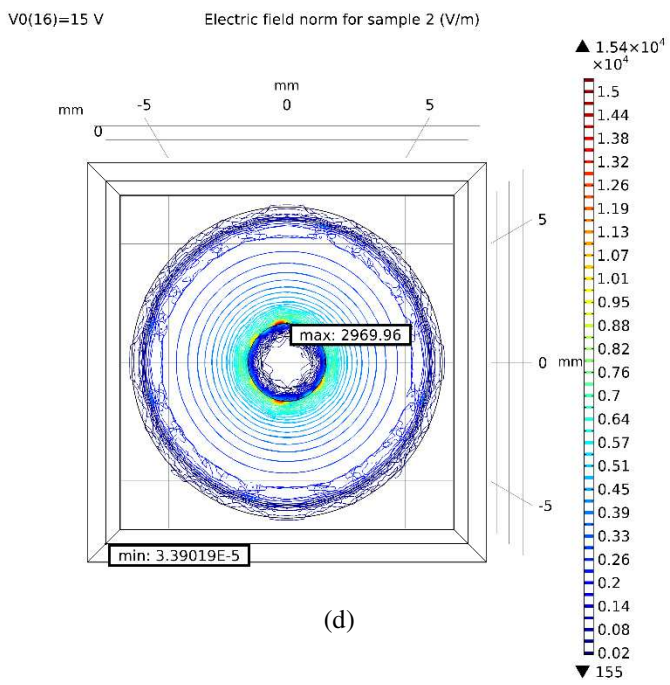
V0(16)=15 V
Electric field norm for sample 2 (V/m)
mm
-5
0
5
max: 2969.96
min: 3.39019E-5
▲ 1.54×10^4
×10^4
1.5
1.44
1.38
1.32
1.26
1.19
1.13
1.07
1.01
0.95
0.88
0.82
0.76
0.7
0.64
0.57
0.51
0.45
0.39
0.33
0.26
0.2
0.14
0.08
0.02
▼ 155

(d)

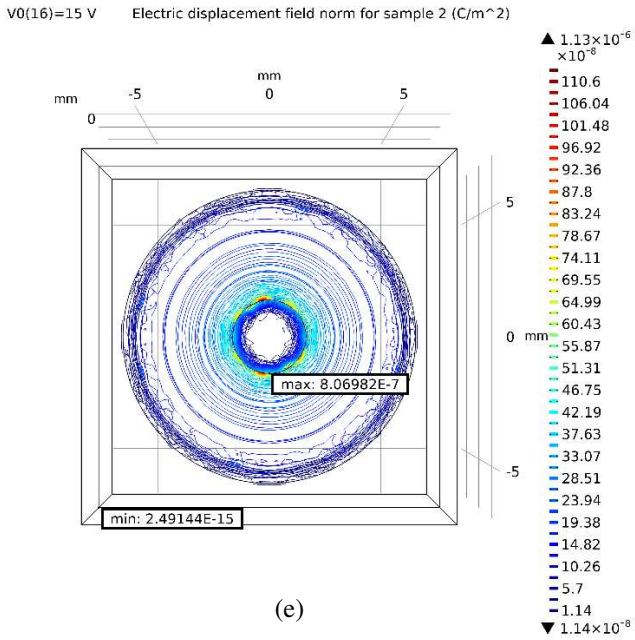
V0(16)=15 V
Electric displacement field norm for sample 2 (C/m^2)
mm
-5
0
5
max: 8.06982E-7
min: 2.49144E-15
▲ 1.13×10^-6
×10^-8
110.6
106.04
101.48
96.92
92.36
87.8
83.24
78.67
74.11
69.55
64.99
60.43
55.87
51.31
46.75
42.19
37.63
33.07
28.51
23.94
19.38
14.82
10.26
5.7
1.14
▼ 1.14×10^-8

(e)

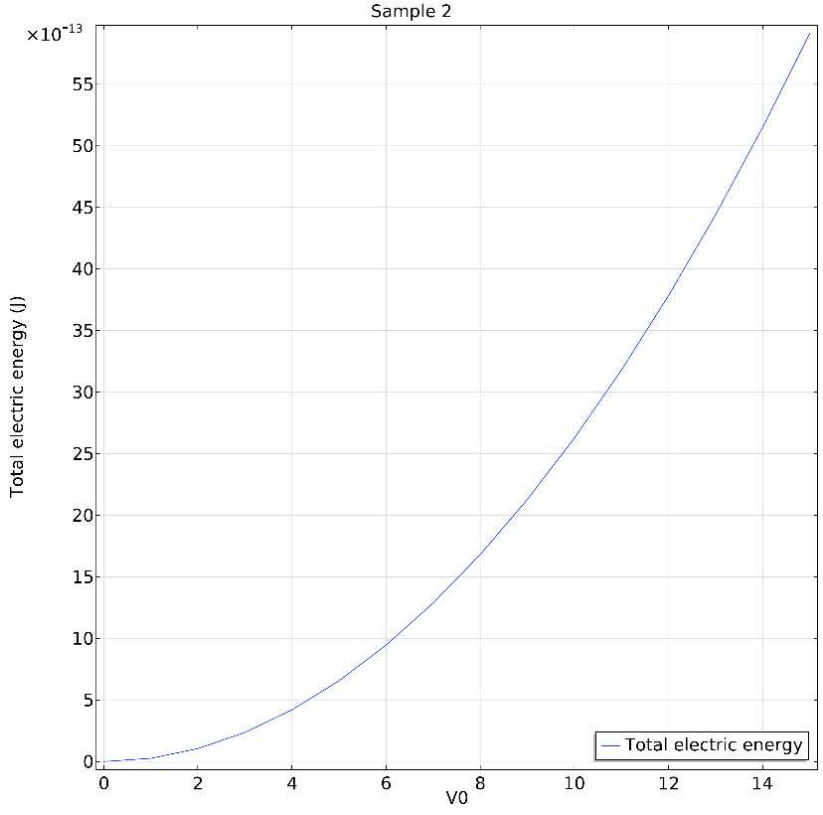
Sample 2
×10^-13
Total electric energy (J)
V0
Total electric energy
0
5
10
15
20
25
30
35
40
45
50
55
0
2
4
6
8
10
12
14

(f)

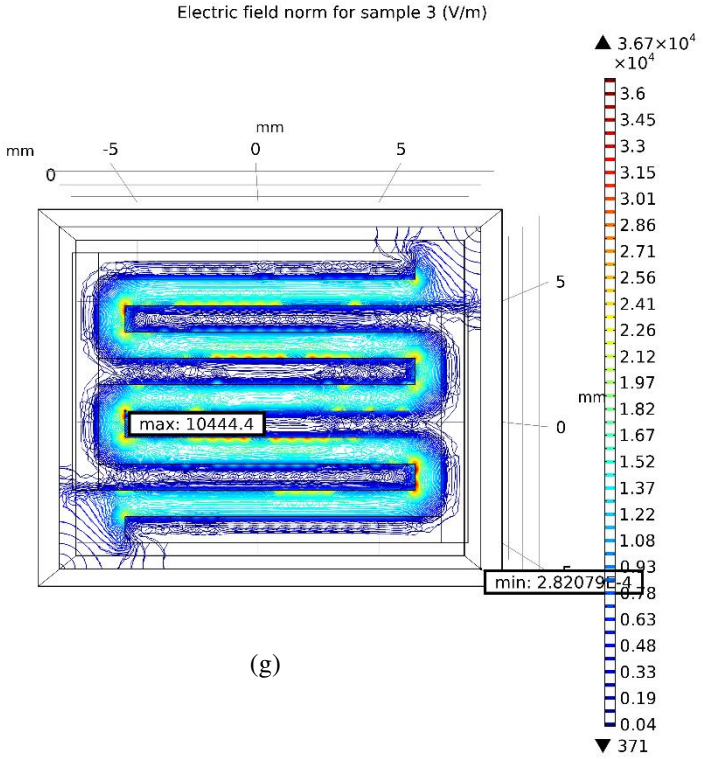
Electric field norm for sample 3 (V/m)
▲ 3.67×10^4
×10^4
3.6
3.45
3.3
3.15
3.01
2.86
2.71
2.56
2.41
2.26
2.12
1.97
1.82
1.67
1.52
1.37
1.22
1.08
0.93
0.78
0.63
0.48
0.33
0.19
0.04
▼ 371
mm
-5
0
5
max: 10444.4
min: 2.82079E-4

(g)

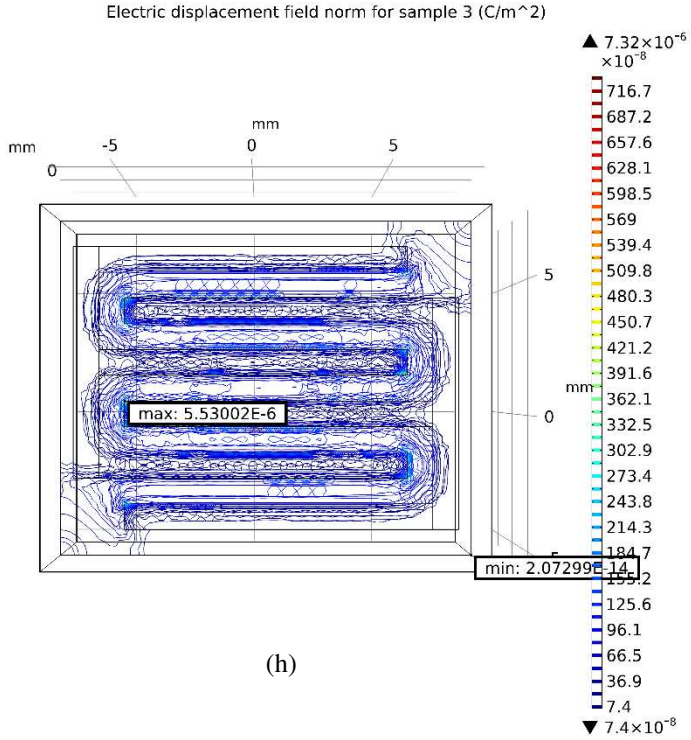
Electric displacement field norm for sample 3 (C/m^2)
▲ 7.32×10^-6
×10^-8
716.7
687.2
657.6
628.1
598.5
569
539.4
509.8
480.3
450.7
421.2
391.6
362.1
332.5
302.9
273.4
243.8
214.3
184.7
155.2
125.6
96.1
66.5
36.9
7.4
▼ 7.4×10^-8
mm
-5
0
5
max: 5.53002E-6
min: 2.07299E-14

(h)

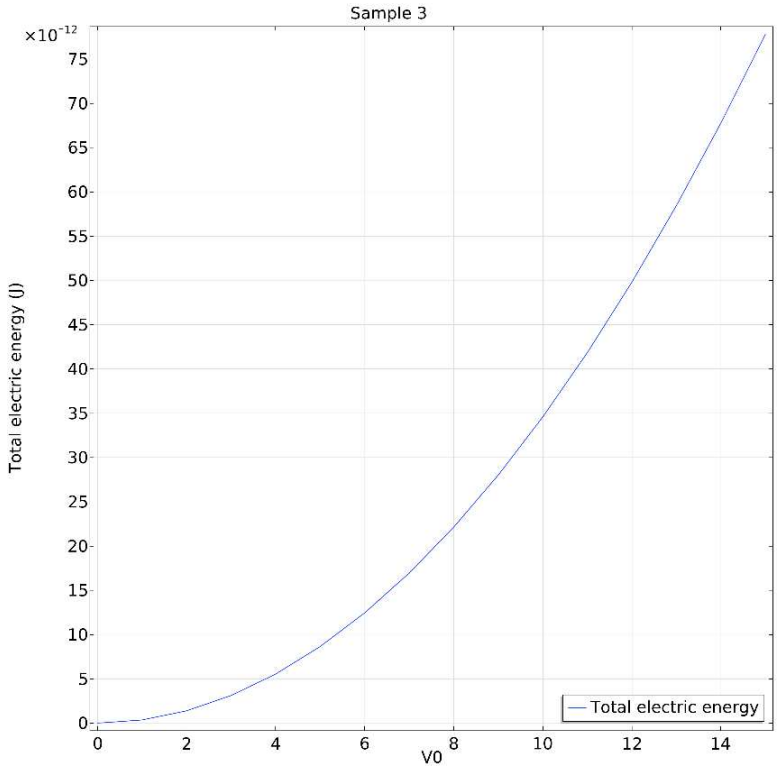
Sample 3
×10^-12
Total electric energy (J)
V0
Total electric energy

(i)

Fig.9: Simulation in COMSOL multiphysics software (a) Electric field norm for sample 1 at 15 V bias (b) Electric displacement field norm for sample 1 at 15 V bias (c) Total electric energy for sample 1 at 0 to 15 V bias (d) Electric field norm for sample 2 at 15 V bias (e) Electric displacement field norm for sample 2 at 15 V bias (f) Total electric energy for sample 2 at 0 to 15 V bias (g) Electric field norm for sample 3 at 15 V bias (h) Electric displacement field norm for sample 3 at 15 V bias (i) Total electric energy for sample 3 at 0 to 15 V bias

For response time, photogenerated carriers move faster with a drift speed due to the electric field, which improves the photon flow and causes higher response speeds. The point is that for the response time because there is illuminated, due to the Schottky barrier and the local potential difference is also involved, the response time (ms) at bias 5 V for these PDs are:

t_{r1} (440) < t_{r3} (570) < t_{r2} (610)

Table 1: Reverse saturation current, Schottky barrier's height, dark current at 15 V, photocurrent at 0, 15 V and rise time for samples

Name	**I_0 (A)**	**ϕ_{Big} (eV)**	**ϕ_{Small} (eV)**	**I_{dark} at 15 V (µA)**	**I_{photo}15 V (µA)**	**I_{photo} at 0V (µA)**	**t_r (ms)**
Sample 1	8.232×10^{-7}	0.651	0.619	9.24	470	0.8	440
Sample 2	4.213×10^{-7}	0.668	0.624	5.41	18.14	0.3	610
Sample3	4.244×10^{-6}	0.614	0.614	67.3	208	0	570

In short, if only the difference between the Schottky barrier is considered, sample 2, sample 1, and finally sample 3, respectively, had the largest difference (using MATLAB software). If only the shape and amount of electric field are considered, the maximum value should be for sample 3, then sample 1, and finally sample 2 (with COMSOL multiphysics software). While both of these factors must be considered together, and when both are considered together, it can be seen that in sample

1, a difference in the Schottky barrier leads to local potential and thus to a local electric field. It can be prepared with the help of the main electric field and surpass the photocurrent of sample 1 from sample 3. In sample 2, because the electric field amount was much lower, this local electric field could not compensate for this shortage.

4. Conclusion:

In this study, the effect of electrode shape on the parameters of flexible UV PDs based on porous ZnO on the fiberglass (Fr4) substrate was investigated. It was observed that the difference in the height of the Schottky barrier could be the basis for the creation of self-powered PDs. Also, the shape of the electrodes affects the amount and shape of the electric field created, which is the transfer factor of the charge carriers, which leads to a change in the output current of the PDs. Among these 3 PDs, which were fabricated simultaneously using RF sputtering and PCB techniques, sample 1 was the best in the current at 0 V (0.8 µA), the photocurrent (at 15 V=470µA) and the response time (440 ms). From experimental data and information obtained from computing and simulation software (MATLAB and COMSOL multiphysics), it can be concluded that the output currents of the PDs in illuminated are related to the difference of potentials and electric fields created. These samples are different in two ways: first, the difference in local potential due to the difference in the height of the Schottky barrier, and second, the difference in shape and amount of electric field due to the difference in the shape of the electrodes. Between these 3 PDs, sample 1 with two circular and rectangular electrodes showed the best performance under illuminated conditions (both at 0 volts and in bias mode).

References:

[1] Y. Pei, R. Pei, X. Liang, Y. Wang, L. Liu, H. Chen, J. Liang, CdS-nanowires flexible photo-detector with Ag-nanowires electrode based on non-transfer process, Scientific reports 6 (2016) 21551.

[2] J. Gao, W.-J. Liu, S.-J. Ding, H.-L. Lu, D.W. Zhang, High performance ultraviolet photodetectors with atomic-layer-deposited ZnO films via low-temperature post-annealing in air, AIP Advances 8(1) (2018) 015015.
[3] B. Efafi, H. Mazandarani, M.H.M. Ara, B. Ghafary, Improvement in photoluminescence behavior of well-aligned ZnO nanorods by optimization of thermodynamic parameters, Physica B: Condensed Matter 579 (2020) 411915.
[4] B. Efafi, S.S. Mousavi, M.H. Majlesara, B. Ghafary, B. Sajad, Fabrication of high-performance UVC photodiodes by Al+ 3 ion adjustment in AZO/Si Heterostructures, Optical Materials 81 (2018) 7-11.
[5] S.S. Mousavi, A. Kazempour, B. Efafi, M.H.M. Ara, B. Sajad, Effects of graphene quantum dots interlayer on performance of ZnO-based photodetectors, Applied Surface Science 493 (2019) 1187-1194.
[6] B. Efafi, S.S. Mousavi, M.H.M. Ara, B. Ghafari, H.R. Mazandarani, A method for optimizing the electrical conductivity of Al: ZnO TCO films, Materials Letters 195 (2017) 52-54.
[7] B. Efafi, M.S. Ghamsari, M. Aberoumand, M.M. Ara, A.S. Ghamsari, H.H. Rad, Aluminum doped ZnO sol–gel derived nanocrystals: Raman spectroscopy and solid solubility characterization, physica status solidi (a) 211(10) (2014) 2426-2430.
[8] G.K. Upadhyay, V. Kumar, L. Purohit, Optimized CdO: TiO2 nanocomposites for heterojunction solar cell applications, Journal of Alloys and Compounds (2020) 157453.
[9] C. Ozcan, D. Turkay, S. Yerci, Optical and electrical design guidelines for ZnO/CdS nanorod-based CdTe solar cells, Optics express 27(8) (2019) A339-A351.
[10] S.S. Taleghani, M.R.Z. Meymian, M. Ameri, Interfacial modification to optimize stainless steel photoanode design for flexible dye sensitized solar cells: an experimental and numerical modeling approach, Journal of Physics D: Applied Physics 49(40) (2016) 405601.
[11] K. Liu, M. Sakurai, M. Aono, ZnO-based ultraviolet photodetectors, Sensors 10(9) (2010) 8604-8634.
[12] S.S. Mousavi, B. Sajad, B. Efafi, H. Alaibakhsh, K.E. Jahromi, M.H. Majlesara, B. Ghafary, Practical optimization of highly sensitive azo photoconductor with circular electrode scheme, Journal of Lightwave Technology 36(24) (2018) 5800-5806.
[13] T.K. Pathak, V. Kumar, H. Swart, L. Purohit, P-type conductivity in doped and codoped ZnO thin films synthesized by RF magnetron sputtering, Journal of Modern Optics 62(17) (2015) 1368-1373.
[14] M. Ameri, M. Raoufi, M.-R. Zamani-Meymian, F. Samavat, M.-R. Fathollahi, E. Mohajerani, Self-assembled ZnO nanosheet-based spherical structure as photoanode in dye-sensitized solar cells, Journal of Electronic Materials 47(3) (2018) 1993-1999.
[15] Q. An, X. Meng, K. Xiong, Y. Qiu, Self-powered ZnS nanotubes/Ag nanowires MSM UV photodetector with high on/off ratio and fast response speed, Scientific Reports 7(1) (2017) 1-12.
[16] K. Liu, D. Shen, C. Shan, J. Zhang, B. Yao, D. Zhao, Y. Lu, X. Fan, Zn 0.76 Mg 0.24 O homojunction photodiode for ultraviolet detection, Applied Physics Letters 91(20) (2007) 201106.
[17] H. Zhu, C. Shan, B. Yao, B. Li, J. Zhang, D. Zhao, D. Shen, X. Fan, High spectrum selectivity ultraviolet photodetector fabricated from an n-ZnO/p-GaN heterojunction, The Journal of Physical Chemistry C 112(51) (2008) 20546-20548.
[18] Y.Q. Bie, Z.M. Liao, H.Z. Zhang, G.R. Li, Y. Ye, Y.B. Zhou, J. Xu, Z.X. Qin, L. Dai, D.P. Yu, Self-powered, ultrafast, visible-blind UV detection and optical logical operation based on ZnO/GaN nanoscale p-n junctions, Advanced materials 23(5) (2011) 649-653.
[19] P.A. Shaikh, V.P. Thakare, D.J. Late, S. Ogale, A back-to-back MOS–Schottky (Pt–SiO 2–Si–C–Pt) nano-heterojunction device as an efficient self-powered photodetector: one step fabrication by pulsed laser deposition, Nanoscale 6(7) (2014) 3550-3556.
[20] L. Mandal, N.S. Chaudhari, S. Ogale, Self-powered UV-vis photodetector based on ZnIn2S4/hydrogel interface, ACS Applied Materials & Interfaces 5(18) (2013) 9141-9147.
[21] Z. Wang, S. Ran, B. Liu, D. Chen, G. Shen, Multilayer TiO 2 nanorod cloth/nanorod array electrode for dye-sensitized solar cells and self-powered UV detectors, Nanoscale 4(11) (2012) 3350-3358.
[22] X. Li, C. Gao, H. Duan, B. Lu, X. Pan, E. Xie, Nanocrystalline TiO2 film based photoelectrochemical cell as self-powered UV-photodetector, Nano Energy 1(4) (2012) 640-645.

[23] Y. Xie, L. Wei, G. Wei, Q. Li, D. Wang, Y. Chen, S. Yan, G. Liu, L. Mei, J. Jiao, A self-powered UV photodetector based on TiO 2 nanorod arrays, Nanoscale research letters 8(1) (2013) 188.
[24] H.-Y. Chen, K.-W. Liu, X. Chen, Z.-Z. Zhang, M.-M. Fan, M.-M. Jiang, X.-H. Xie, H.-F. Zhao, D.-Z. Shen, Realization of a self-powered ZnO MSM UV photodetector with high responsivity using an asymmetric pair of Au electrodes, Journal of Materials Chemistry C 2(45) (2014) 9689-9694.
[25] D. Li, X. Sun, H. Song, Z. Li, H. Jiang, Y. Chen, G. Miao, B. Shen, Effect of asymmetric Schottky barrier on GaN-based metal-semiconductor-metal ultraviolet detector, Applied Physics Letters 99(26) (2011) 261102.
[26] J.-H. Park, H.-Y. Yu, Dark current suppression in an erbium–germanium–erbium photodetector with an asymmetric electrode area, Optics letters 36(7) (2011) 1182-1184.
[27] M. Peng, Y. Liu, A. Yu, Y. Zhang, C. Liu, J. Liu, W. Wu, K. Zhang, X. Shi, J. Kou, Flexible self-powered GaN ultraviolet photoswitch with piezo-phototronic effect enhanced on/off ratio, ACS nano 10(1) (2016) 1572-1579.
[28] S. Liu, M. Sakai, B. Liu, C. Terashima, K. Nakata, A. Fujishima, Facile synthesis of transparent superhydrophobic titania coating by using soot as a nanoimprint template, Rsc Advances 3(45) (2013) 22825-22829.
[29] H. Liu, T. Ye, C. Mao, Fluorescent carbon nanoparticles derived from candle soot, Angewandte chemie 119(34) (2007) 6593-6595.
[30] Y. Cao, S. Deng, Q. Hu, Q. Zhong, Q.-P. Luo, L. Yuan, J. Zhou, Three-dimensional ZnO porous films for self-cleaning ultraviolet photodetectors, RSC advances 5(104) (2015) 85969-85973.
[31] R.A. Ismail, Fabrication and characterization of photodetector based on porous silicon, e-Journal of Surface Science and Nanotechnology 8 (2010) 388-391.
[32] P. Sharma, A. Mansingh, K. Sreenivas, Ultraviolet photoresponse of porous ZnO thin films prepared by unbalanced magnetron sputtering, Applied physics letters 80(4) (2002) 553-555.
[33] L. Dong, J. Yu, R. Jia, J. Hu, Y. Zhang, J. Sun, Self-powered MSM deep-ultraviolet β-Ga 2 O 3 photodetector realized by an asymmetrical pair of Schottky contacts, Optical Materials Express 9(3) (2019) 1191-1199.
[34] A.S. Zoolfakar, R.A. Rani, A.J. Morfa, S. Balendhran, A.P. O'Mullane, S. Zhuiykov, K. Kalantar-zadeh, Enhancing the current density of electrodeposited ZnO–Cu 2 O solar cells by engineering their heterointerfaces, Journal of Materials Chemistry 22(40) (2012) 21767-21775.
[35] L. Rajan, C. Periasamy, V. Sahula, Structural and optical characteristics of RF sputtered ZnO thinfilm on Si substrate for device applications, 2015 Annual IEEE India Conference (INDICON), IEEE, 2015, pp. 1-4.
[36] J. Singh, S. Ranwa, J. Akhtar, M. Kumar, Growth of residual stress-free ZnO films on SiO2/Si substrate at room temperature for MEMS devices, AIP Advances 5(6) (2015) 067140.
[37] A. Djurišić, A.M.C. Ng, X. Chen, ZnO nanostructures for optoelectronics: Material properties and device applications, Progress in quantum electronics 34(4) (2010) 191-259.
[38] S.M. Sze, Semiconductor devices: physics and technology, John wiley & sons2008.
[39] B. Nie, J.G. Hu, L.B. Luo, C. Xie, L.H. Zeng, P. Lv, F.Z. Li, J.S. Jie, M. Feng, C.Y. Wu, Monolayer Graphene Film on ZnO Nanorod Array for High-Performance Schottky Junction Ultraviolet Photodetectors, Small 9(17) (2013) 2872-2879.
[40] J. Liu, C. Shan, B. Li, Z. Zhang, C. Yang, D. Shen, X. Fan, High responsivity ultraviolet photodetector realized via a carrier-trapping process, Applied Physics Letters 97(25) (2010) 251102.
[41] X. Xie, Z. Zhang, B. Li, S. Wang, M. Jiang, C. Shan, D. Zhao, H. Chen, D. Shen, Enhanced solar-blind responsivity of photodetectors based on cubic MgZnO films via gallium doping, Optics Express 22(1) (2014) 246-253.
[42] N. Jandow, H.A. Hassan, F. Yam, K. Ibrahim, ZnO Metal-Semiconductor-Metal UV Photodetectors on PPC Plastic with Various Metal Contacts, Photodetectors (2012) 1-32.
[43] J. Freeouf, T. Jackson, S. Laux, J. Woodall, Effective barrier heights of mixed phase contacts: Size effects, Applied Physics Letters 40(7) (1982) 634-636.

[44] G. Smit, S. Rogge, T. Klapwijk, Scaling of nano-Schottky-diodes, Applied Physics Letters 81(20) (2002) 3852-3854.
[45] C. Donolato, Approximate analytical solution to the space charge problem in nanosized Schottky diodes, Journal of applied physics 95(4) (2004) 2184-2186.
[46] H. Chen, X. Sun, D. Yao, X. Xie, F. Ling, S. Su, Back-to-back asymmetric Schottky-type self-powered UV photodetector based on ternary alloy MgZnO, Journal of Physics D: Applied Physics 52(50) (2019) 505112.
[47] L. Wang, Z. Ju, J. Zhang, J. Zheng, D. Shen, B. Yao, D. Zhao, Z. Zhang, B. Li, C. Shan, Single-crystalline cubic MgZnO films and their application in deep-ultraviolet optoelectronic devices, Applied Physics Letters 95(13) (2009) 131113.
[48] D.C. Look, Recent advances in ZnO materials and devices, Materials Science and Engineering: B 80(1-3) (2001) 383-387.
[49] D.L. Rogers, Integrated optical receivers using MSM detectors, Journal of lightwave technology 9(12) (1991) 1635-1638.
[50] Q. Zheng, F. Huang, K. Ding, J. Huang, D. Chen, Z. Zhan, Z. Lin, MgZnO-based metal-semiconductor-metal solar-blind photodetectors on ZnO substrates, Applied Physics Letters 98(22) (2011) 221112.
[51] F.F. Masouleh, N. Das, Application of metal-semiconductor-metal photodetector in high-speed optical communication systems, InTech2014.

Highlights:

- The shape of the electrode affects the amount and distribution of the electric field.
- Photodiode with rectangular and circular electrodes produces the most photocurrent.
- Asymmetric electrodes lead to Schottky barrier difference and create electric field.

Figures

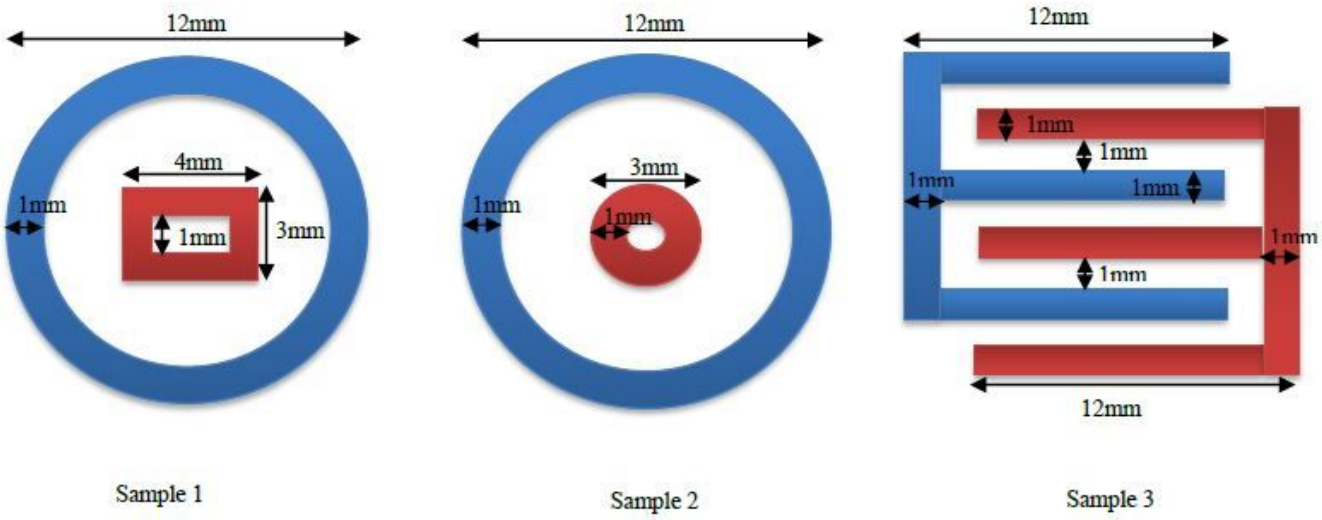

Figure 1

Dimensions of PD electrodes

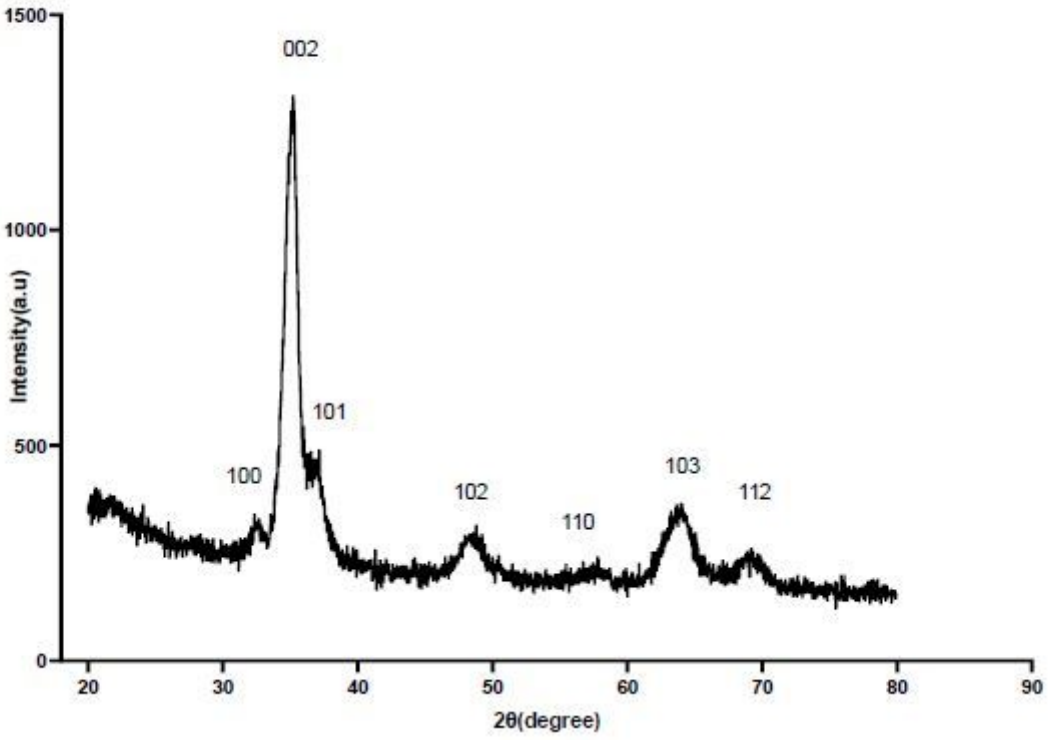

Figure 2

XRD Pattern of flexible UV PDs based on ZnO on the fiberglass (FR4) substrate

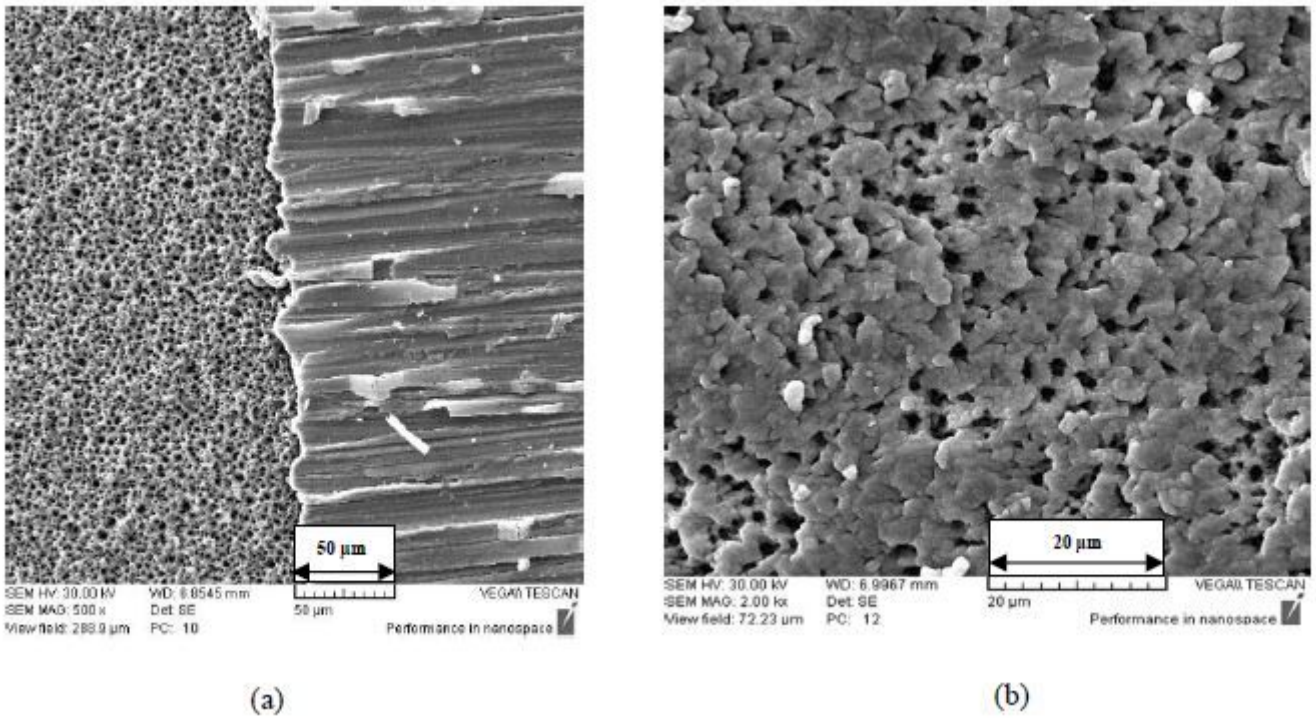

Figure 3

SEM image of flexible UV PDs based on ZnO on the fiberglass (FR4) substrateat (a) at ×500 magnification of electrode and ZnO together, (b) at ×2 K magnification of ZnO

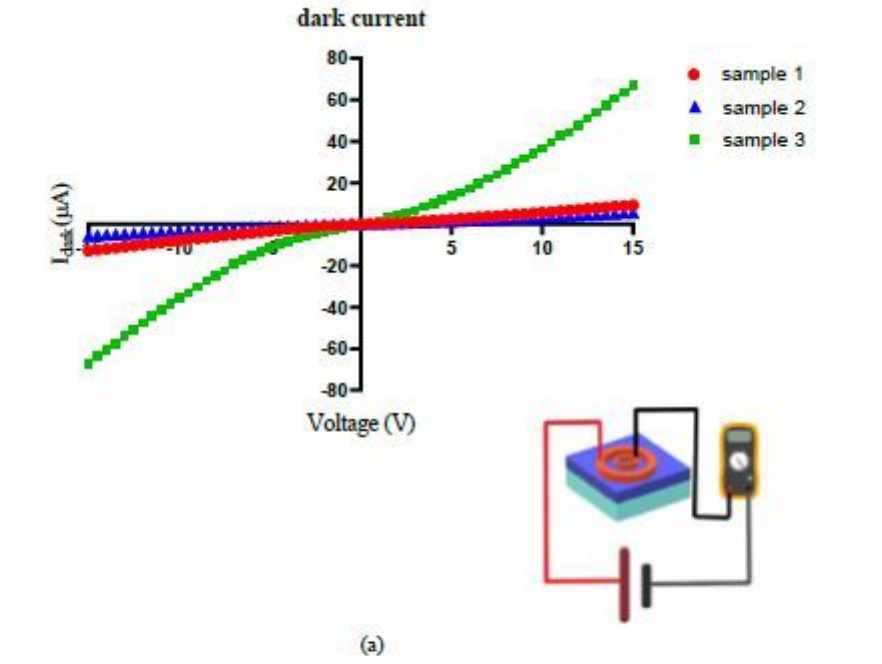

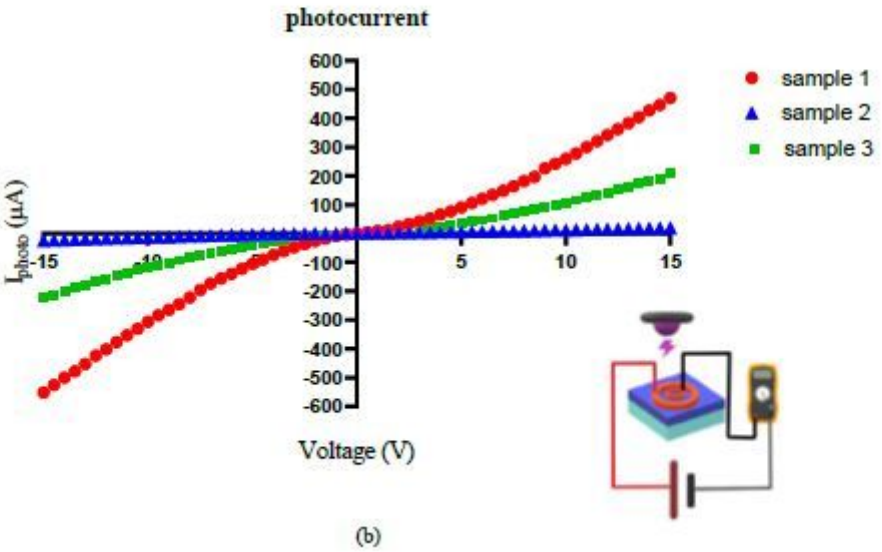

Figure 4

(a) dark current (b) photocurrent of flexible UV PDs based on ZnO on the fiberglass (FR4) substrate

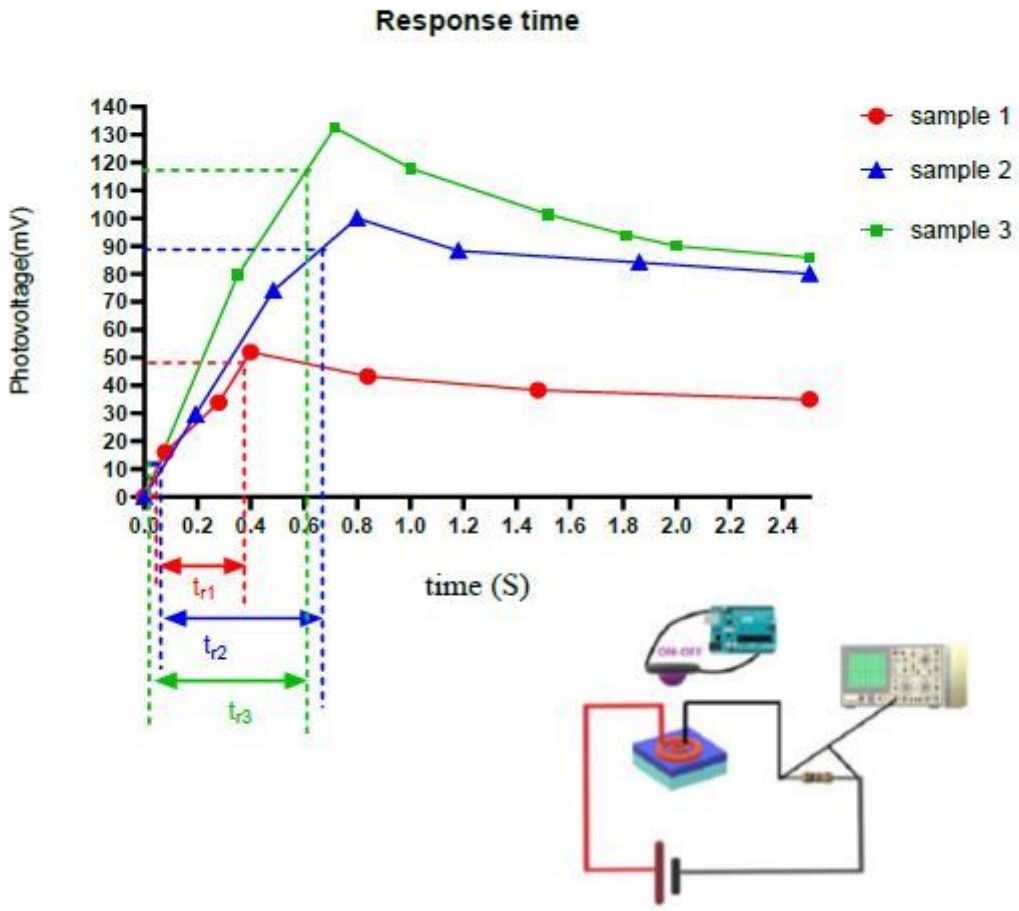

Figure 5

response time of flexible UV PDs based on ZnO on the fiberglass (FR4) substrate

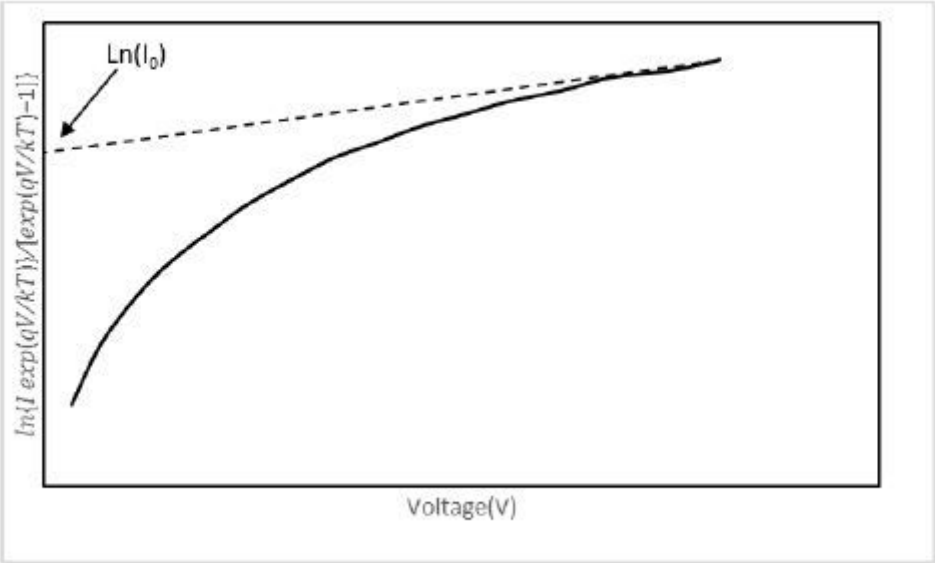

Figure 6

please see the manuscript file for the full caption

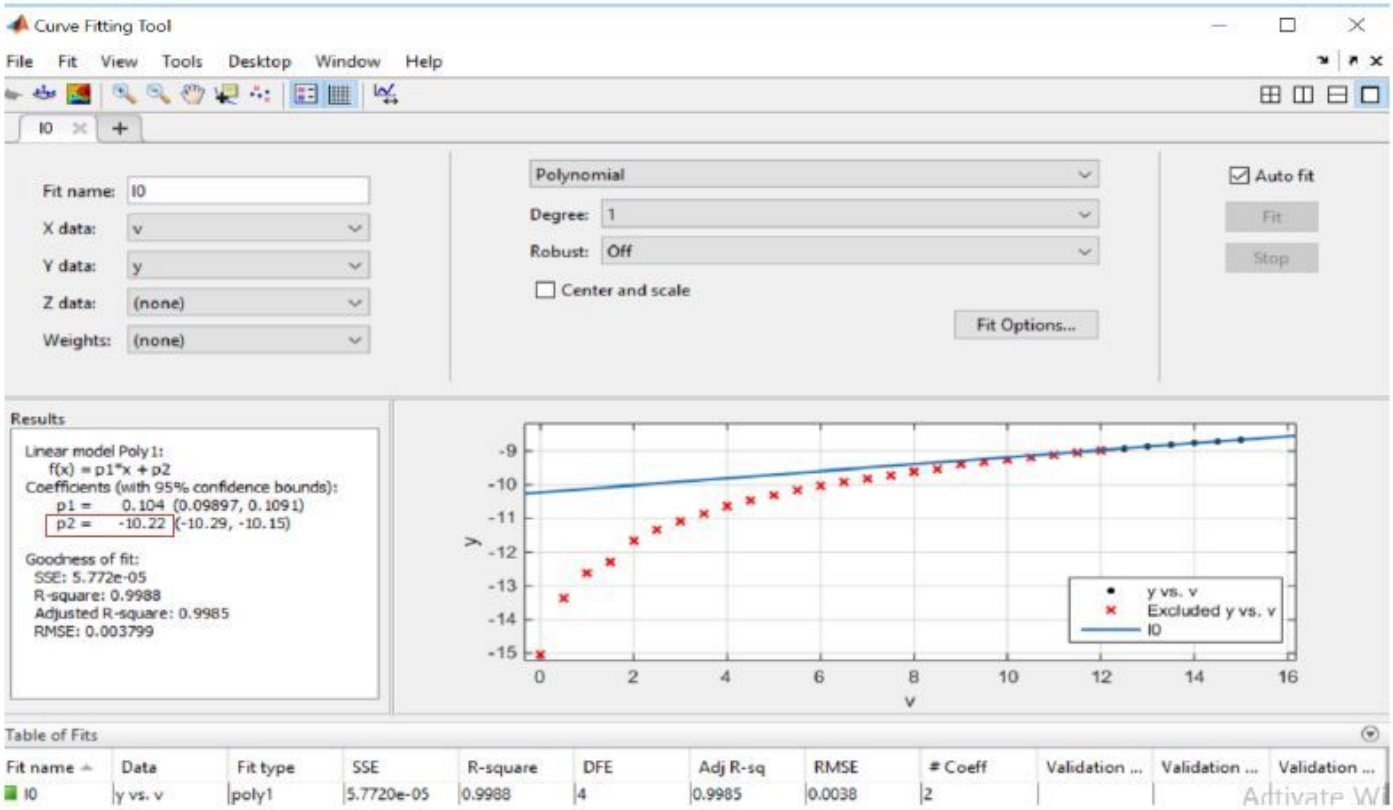

Figure 7

curve fitting in MATLAB software and obtain Ln (I0)

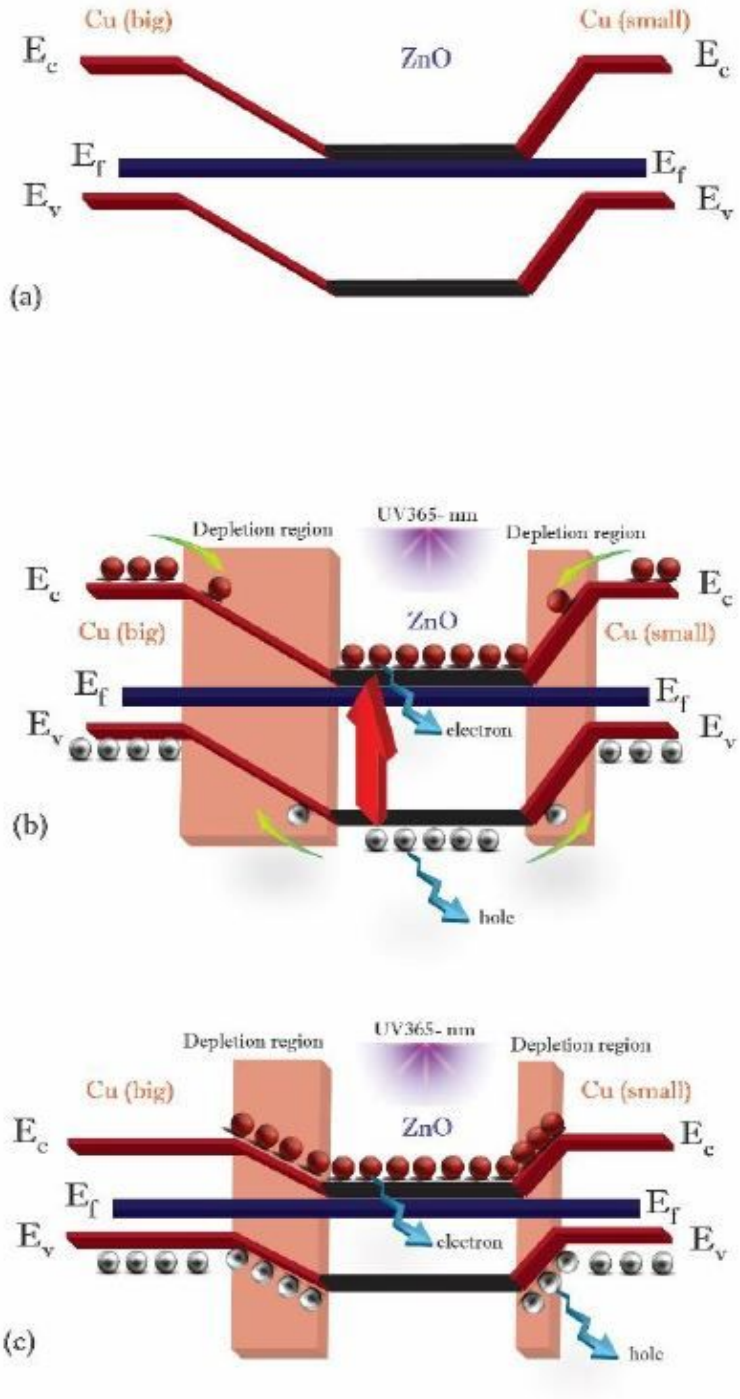

Figure 8

Energy band diagrams of the asymmetric MSM PD at 0 V in the (a) dark and (b, c) illuminated

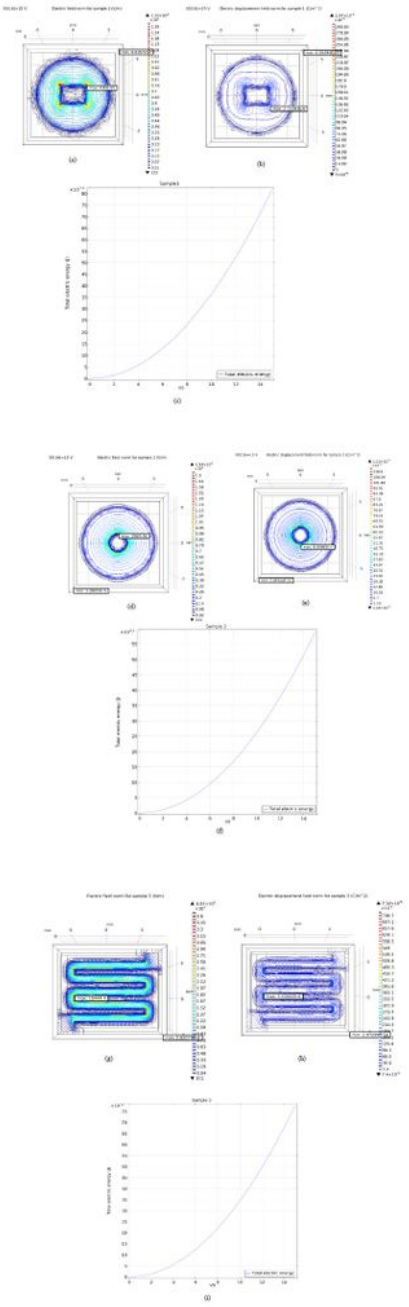

Figure 9

Simulation in COMSOL multiphysics software (a) Electric field norm for sample 1 at 15 V bias (b) Electric displacement field norm for sample 1 at 15 V bias (c) Total electric energy for sample 1 at 0 to 15 V bias (d) Electric field norm for sample 2 at 15 V bias (e) Electric displacement field norm for sample 2 at 15 V bias (f) Total electric energy for sample 2 at 0 to 15 V bias (g) Electric field norm for sample 3 at 15 V

bias (h) Electric displacement field norm for sample 3 at 15 V bias (i) Total electric energy for sample 3 at 0 to 15 V bias